A&A 379, 501–514 (2001)
DOI: 10.1051/0004-6361:20011278

Astronomy & Astrophysics

Qualitative reproduction of stellar H_2O maser morphology

I. Results at a single stellar phase

E. M. L. Humphreys[1], J. A. Yates[2], M. D. Gray[3], D. Field[4], and G. H. Bowen[5]

[1] Onsala Space Observatory, 43992 Onsala, Sweden
[2] Department of Physics and Astronomy, UCL, Gower Street, London WC1E 6BT, UK
e-mail: jyates@star.ucl.ac.uk
[3] Department of Physics, UMIST, PO Box 88, Manchester M60 1QD, UK
e-mail: mdg@saturn.phy.umist.ac.uk
[4] Institute for Storage Ring Facilities, University of Aarhus, 8000 Aarhus C, Denmark
e-mail: dfield@ifa.au.dk
[5] Department of Physics and Astronomy, Iowa State University, Ames IA 50011-3160, USA
e-mail: ghbowen@iastate.edu

Received 9 May 2001 / Accepted 11 September 2001

Abstract. We attempt to reproduce the observed morphologies of stellar H_2O maser emission by combining a hydrodynamic pulsation model of a long-period variable (LPV) star with an H_2O maser model. These numerical simulations yield synthetic maser lineshapes and interferometry images as a function of stellar pulsation phase. The results at a single stellar phase are presented here for 22, 321, 325 and 183 GHz masers. We compare our simulated data with the observed features of stellar H_2O masers, and make predictions of the existence of new masers in the circumstellar environment. We also predict the appearance of 183, 321 and 325 GHz maser images which may be observable in future using the Atacama Large Millimetre Array (ALMA). These simulations correctly locate the shell of 22 GHz masers in the region of the circumstellar envelope (CE) in which material is being accelerated to form the steadily-outflowing stellar wind.

Key words. masers – radiative transfer – stars: AGB and post-AGB – stars: mass-loss – hydrodynamics – circumstellar matter

1. Introduction

MERLIN and VLA data have provided the evidence that stellar H_2O maser emission at 22 GHz is located in a shell expanding from LPV stars (e.g. Reid & Menten 1990; Bowers & Johnston 1994; Yates et al. 1994; Colomer et al. 2000). The shell appears clumpy and incomplete at these resolutions. Emission originates from the inner parts of the CE of Mira-type stars, from regions of diameter $4{-}7 \times 10^{14}$ cm, which are comparable in extent to those in which dust grains form and grow, and in which the expanding envelope has not yet reached terminal velocity. 22 GHz masers are believed to probe circumstellar gas in which acceleration away from the star takes place via radiation pressure on dust and subsequent gas-grain collisions (Chapman & Cohen 1986).

Other H_2O masers are well-known to exist in the evolved circumstellar environment, see Table 1. For example, maser emission at 321, 325 and 183 GHz is common (Menten et al. 1990; Menten & Melnick 1991; Yates et al. 1995; González-Alfonso et al. 1998). However, all information about the location of these masers in the CE must be inferred from spectral line profiles at present. Their use as tools for probing circumstellar conditions has therefore been limited. Knowledge of the location of common stellar H_2O masers in the CE could make them especially useful for deducing the precise evolutionary stage of the star, in combination with other maser observations (Lewis 1989). We note that, in the case of H_2O masers, the type of line profiles observed also provide a good indication of the evolutionary status of the LPV star (e.g. Takaba et al. 1994).

In this paper, we combine a hydrodynamic pulsation model of a LPV of relatively low mass loss rate, a Mira-type variable, with an H_2O maser propagation model. The aim of this work is to reproduce the observed features of stellar H_2O masers, to investigate the physical conditions leading to such emission and to predict the spatial

Send offprint requests to: E. M. L. Humphreys,
e-mail: liz@oso.chalmers.se

Table 1. Astrophysical H_2O masers detected to date. G = ground vibrational state; ν_2 = vibrationally excited bending mode; O, P = ortho or para-H_2O; E_u = energy of the upper level of the masing transition above ground state.

Transition	v-state	Ortho/ Para	ν (GHz)	E_u/k (K)
$6_{16} \rightarrow 5_{23}$	G	O	22	644
$4_{40} \rightarrow 5_{33}$	ν_2	P	96	3060
$3_{13} \rightarrow 2_{20}$	G	P	183	205
$5_{50} \rightarrow 6_{43}$	ν_2	O	232	3451
$10_{29} \rightarrow 9_{36}$	G	O	321	1863
$5_{15} \rightarrow 4_{22}$	G	P	325	470
$17_{4\,13} \rightarrow 16_{7\,10}$	G	O	355	5786
$4_{14} \rightarrow 3_{21}$	G	O	380*	324
$7_{53} \rightarrow 6_{60}$	G	P	437	1526
$6_{43} \rightarrow 5_{50}$	G	O	439	1089
$6_{42} \rightarrow 5_{51}$	G	P	471	1091
$1_{10} \rightarrow 1_{01}$	ν_2	O	658	2361

* Has never been observed towards a stellar environment.

structure of the submillimetre masers in the CE before the advent of ALMA.

We note that the performance of these simulations depends on the accuracy of current LPV stellar pulsation and maser models. The pulsation model, which was developed by Prof. G. Bowen and is based on Bowen (1988), loses mass at a rate of $\dot{M} = 1.8 \times 10^{-7}\ M_\odot\ \mathrm{yr}^{-1}$, mainly through a combination of stellar pulsation-driven shock waves and radiation pressure on dust. The maser saturation radiation transport model was developed by Dr. J. Yates, and is based on Doel et al. (1995) and Gray et al. (1995). These models are described in Sect. 2. Observational data for stellar H_2O masers are described and compared with the results of our simulations in Sects. 3, 4 and 5.

2. Modelling method

The method of modelling stellar H_2O maser emission at a single stellar phase of the pulsation cycle of a LPV star is analogous to that used in the stellar SiO maser model of Humphreys et al. (1996) (H96). The hydrodynamic stellar model employed here is the pulsating CE of a M-Mira variable. It is identical to that detailed in Sect. 3 of H96, except that in the present work we have extrapolated the model beyond its outer radial boundary of 53 AU to 134 AU using the radial dependency derived from the Bowen data. We therefore do not describe the stellar model in detail again here. The model star has the characteristics given in Table 2. We note that a stellar radius of 244 $R_\odot$ (1.1 AU) is rather small when compared with values typically measured for M-Mira variables, at around 2 AU. However, our model star is similar in size and in $\dot{M}$ to measurements for R Cas (see Sect. 5.1). The physical conditions in the spherically symmetric CE at the epoch of our calculations are shown in Fig. 1. We outline the overall procedure for coupling the H_2O maser model to the CE model, and give details of the H_2O maser model, in Sects. 2.1 and 2.2 respectively.

2.1. Overview of the single epoch model

It is evident from the observational data at 22 GHz that only certain regions at the same radius in the CE are suitable for the formation of bright masers. In order to mimic the clumpy nature of the CE, the cause of which is unknown, we must break the spherical symmetry of our CE model. At the epoch of the stellar cycle chosen for our calculations, we follow the procedure described below.

(i) Sites of potential maser action are distributed in the model CE by a standard Monte Carlo method. We require a distribution of sites which has a lower filling factor with increasing distance from the star, in order to imitate a scenario in which water maser clumps are produced near to the star and then travel out to occupy shells of larger volume. This is based on observational data in Richards et al. (1999), and is realised by a uniform distribution of sites over radial distance, r, a distribution of polar angle θ' which is related to a randomly chosen value of θ between 0 and π of $\theta' = \cos^{-1}(1 - 2\theta/\pi)$, and a uniform distribution of azimuthal angle, ϕ. H_2O maser emission is calculated at these Monte Carlo sites only, at which the abundance of H_2O is assumed to be $n(H_2O)/n(H_2) = 10^{-4}$. On the basis of trial calculations, 3000 sites are used in the current model between the radial limits of 1–50 R_* (1.13–56.5 AU) from the centre of the star. 3000 sites were chosen in order to yield the number of bright components observed towards evolved stars. The outer radial boundary was chosen such that no inversions for any H_2O maser transitions were found to occur beyond this distance.

(ii) The physical conditions at each maser site are derived from the CE model. r defines the physical conditions at the site, whereas θ' and ϕ are necessary (i) to calculate the line-of-sight velocity gradient, α_{los}, at r (Eq. (4) in H96);

Table 2. Characteristics of the model star used to compute the physical conditions in the CE of a typical M-Mira long-period variable.

Parameters of the model M-Mira variable	
Mass	1 $M_\odot$
Fundamental period	332 days
Stellar radius	244 $R_\odot$ (1.7×10^{11} m)
Effective temperature	3002.2 K
Maximum inner boundary speed	3.93 $\mathrm{km\,s^{-1}}$
Mass loss rate	$1.8 \times 10^{-7}\ M_\odot\ \mathrm{yr}^{-1}$

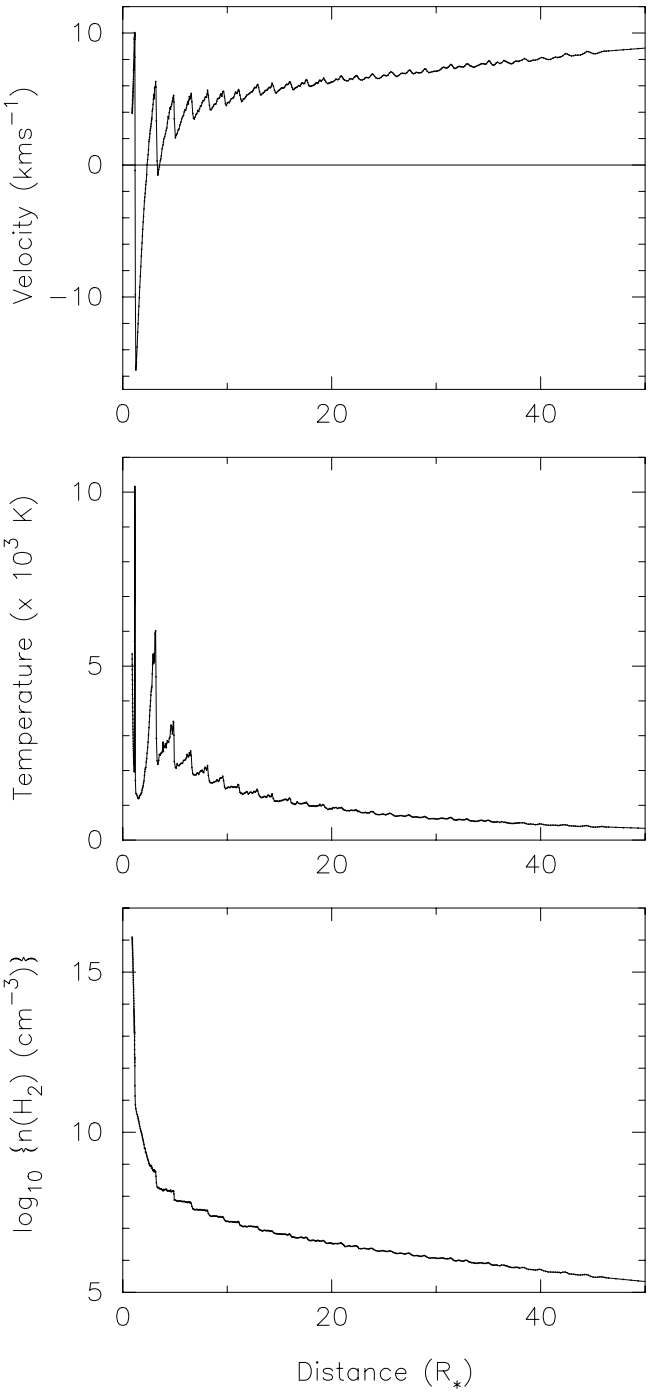

Fig. 1. The physical conditions in the model CE at the epoch of our calculations. **a)** Gas velocity as a function of radial distance; **b)** kinetic temperature, T_k; **c)** hydrogen number density, $n(H_2)$. 1 R_* corresponds to 1.1 AU at this epoch.

and (ii) to define the position, in the plane of the sky, of any maser component which may develop.

(iii) At each site, the population distribution of H_2O molecules over energy states is calculated using the Large Velocity Gradient (LVG) approximation (see Sect. 2.2.2). Where population inversions result for maser transitions, maser radiation is propagated in the line-of-sight.

(iv) The emission from sites which yield masers (we refer to emitting sites as "components" hereafter) is combined to produce single-dish lineshapes and VLBI-type images. Each component produces a spectral emission line corresponding to each maser transition from which emission is calculated to occur. For any given maser transition, the spectral lines from all components are combined at their appropriate line-of-sight velocity to form single-dish lineshapes. In order to produce VLBI-type images, for any given maser transition, the spectral line from each component is averaged over all velocity channels and plotted at its projected coordinates. We emphasise that the success of any maser site for becoming a component depends on the physical conditions found at that site in the CE model and is not constrained to occur in any way. For example, less than half of the 3000 Monte Carlo sites distributed give rise to 22 GHz emission in the line-of-sight (see Sect. 5.1).

2.2. The H_2O maser model

The H_2O maser model consists of 100 rotational energy levels of the ground vibrational states of both ortho and para-H_2O. It is a 1-D radiation transport code in which the radiation field is treated classically and the molecular response is quantum mechanical. The effects of saturation and competitive gain are included in the propagation of maser radiation through a gas which contains population inversions, based on Field & Gray (1988).

2.2.1. Inputs to the model

The r coordinate of a maser site places it in a radial zone of the CE model. Linear interpolation between the boundary values of the zone provides values of the gas kinetic temperature (T_k), density and bulk radial velocity at the site. The radial and line-of-sight velocity gradients at r can be calculated directly, using the θ' and ϕ coordinates of the site, see Sect. 2.2.3. We assume the gas to be composed of molecular hydrogen, with number density $n(H_2)$. Our value of the H_2O abundance (10^{-4}) is based on the models of stellar H_2O abundance by González-Alfonso & Cernicharo (1999). It is also consistent with the range of values of $n(H_2O)$ found to result in population inversions in Yates et al. (1997; Y97 hereafter). We assume a thermal equilibrium ortho-to-para water abundance ratio of 3. The radiation field in the model is described in Sect. 2.2.2. The maser propagation distance is derived from the CE model, see Sect. 2.2.3.

2.2.2. Calculating the populations

Calculation of the H_2O level populations involves the solution of the kinetic master equations for 100 rotational energy levels in the ground vibrational state of both ortho and para-H_2O. Einstein A-values for the 422 dipole-allowed transitions involved are calculated using an

Table 3. Ranges of physical conditions which yield the five brightest components at each frequency. r is the coordinate of the maser site; $\alpha_{\rm los}$ is the velocity gradient along the direction of maser propagation in the line-of-sight; $\partial V/\partial R$ is the bulk radial velocity gradient at r; V/r is the tangential velocity gradient at r.

ν (GHz)	r (cm)	$T_{\rm k}$ (K)	$n(H_2)$ (cm^{-3})	$\mid \alpha_{\rm los} \mid$ ($km\,s^{-1}\ pc^{-1}$)	$\mid \partial V/\partial R \mid$ ($km\,s^{-1}\ pc^{-1}$)	$\mid V/r \mid$ ($km\,s^{-1}\ pc^{-1}$)
22	3.5E13 → 4.6E13	1819 → 4213	9.0E8 → 3.4E9	1.1E5 → 7.1E5	9.0E5 → 2.6E6	1.5E5 → 2.5E5
321	3.5E13 → 5.8E13	1819 → 4007	1.9E8 → 3.4E9	1.9E4 → 1.2E5	5.6E5 → 1.1E7	1.8E4 → 2.8E5
325	3.7E13 → 6.1E13	2070 → 2552	1.7E8 → 2.5E9	1.9E5 → 8.8E5	4.4E5 → 1.8E6	1.3E4 → 2.0E5
183	1.7E14 → 2.2E14	1343 → 1583	1.1E7 → 1.7E7	5.7E4 → 7.4E4	6.5E3 → 3.5E5	7.8E4 → 9.3E4

algorithm described in Bayley (1985). Rate coefficients for inelastic collisions between H_2O and He involving the first 45 levels, up to level 7_{70} for ortho and 7_{71} for para-H_2O, are taken from Green et al. (1993). As we assume the collision partner to be molecular hydrogen rather than helium, the rate coefficients in Green et al. (1993) are scaled to account for the difference in reduced mass. For collisional rate coefficients for which either level lies above 7_{70} and 7_{71}, the rate coefficients are estimated using the parametrisation adopted in Neufeld & Melnick (1991). The radiation field in the model consists of the stellar continuum, suitably spatially diluted according to the radial distance of each maser site from the star, and a dust radiation field. The stellar continuum radiation field is that of a black-body at the effective temperature of the model star. The dust local to the H_2O maser zone is assumed to be at its frequency-dependent radiative equilibrium temperature. The dust temperature is computed using a spherical radiation transport model, using dust opacity data from Laor & Draine (1993). The maser amplifies this background radiation field, which is composed of the dust and the stellar continuum.

To calculate self-consistent populations and line and continuum radiation fields, solutions of the kinetic master equations for the populations of the rotational energy levels of H_2O are obtained using the Sobolev or LVG approximation. We have employed this method, rather than use an accurate Accelerated Lambda Iteration (ALI) method, due to the time constraints imposed by the large number of calculations required to produce this model. In the present work, the LVG method has a further advantage that it provides a size for the maser region which is independent of other parts of the CE, the analogue of the observational clump size. We note that the use of the LVG approximation is rarely appropriate. It is a useful qualitative method, however, when the maser pump scheme is dominated by collisional excitations. The H_2O maser at 22 GHz is well-known to be pumped by such a scheme (see e.g. Y97; Cooke & Elitzur 1985). However, if the pumping requires predominantly radiative excitations, the LVG approximation is no longer an effective method. The drawback here is that the maser lines at 437, 439 and 471 GHz, which are found to have a predominantly radiative pump in Y97 using an ALI method, will be poorly represented by an LVG model and cannot be modelled here. Of the 100 levels included in the calculations for each of ortho- and para-H_2O, we exclude the results from the energy levels higher than 60. The truncation of energy levels may lead to inaccurate line optical depths for the higher levels.

Table 4. Data ranges which result for the five brightest components at each frequency. Fractional saturation distance = saturation distance/propagation distance.

ν (GHz)	Propagation Distance (m)	Fractional Saturation Distance	$FWHM$ ($km\,s^{-1}$)
22	2.98E11 → 1.72E12	0.33 → 0.62	0.98 → 1.47
321	1.75E12 → 3.00E12	0.47 → 0.90	0.92 → 2.67
325	2.42E11 → 1.27E12	0.27 → 0.52	0.94 → 2.71
183	2.50E12 → 3.00E12	0.40 → 0.47	0.84 → 1.00

2.2.3. Maser propagation

Maser radiation is propagated in the line-of-sight for maser transitions in which population inversions are calculated. We identify the line-of-sight by calculating the velocity gradient in the line-of-sight at r, according to Eq. (4) of H96. The length of gas traversed during the amplification process is constrained to have a maximum value of 3×10^{12} m, a distance which has been empirically derived from resolved 22 GHz maser features in RT Vir (Richards, private communication), or a value such that the velocity gradient in our line-of-sight causes a shift of 3 Doppler widths, which ever is the smaller. Field et al. (1994) showed that, in the presence of a velocity gradient along the path of maser propagation, significant amplification may take place for velocity shifts exceeding 1 Doppler width, i.e. for propagation distances greater than $\Delta v_{\rm th}/|\alpha_{\rm los}|$, where $\Delta v_{\rm th}$ is the thermal linewidth and $|\alpha_{\rm los}|$ is the velocity gradient. We note that simulations show that, when the velocity shift exceeds 3 Doppler widths, amplification typically becomes negligible.

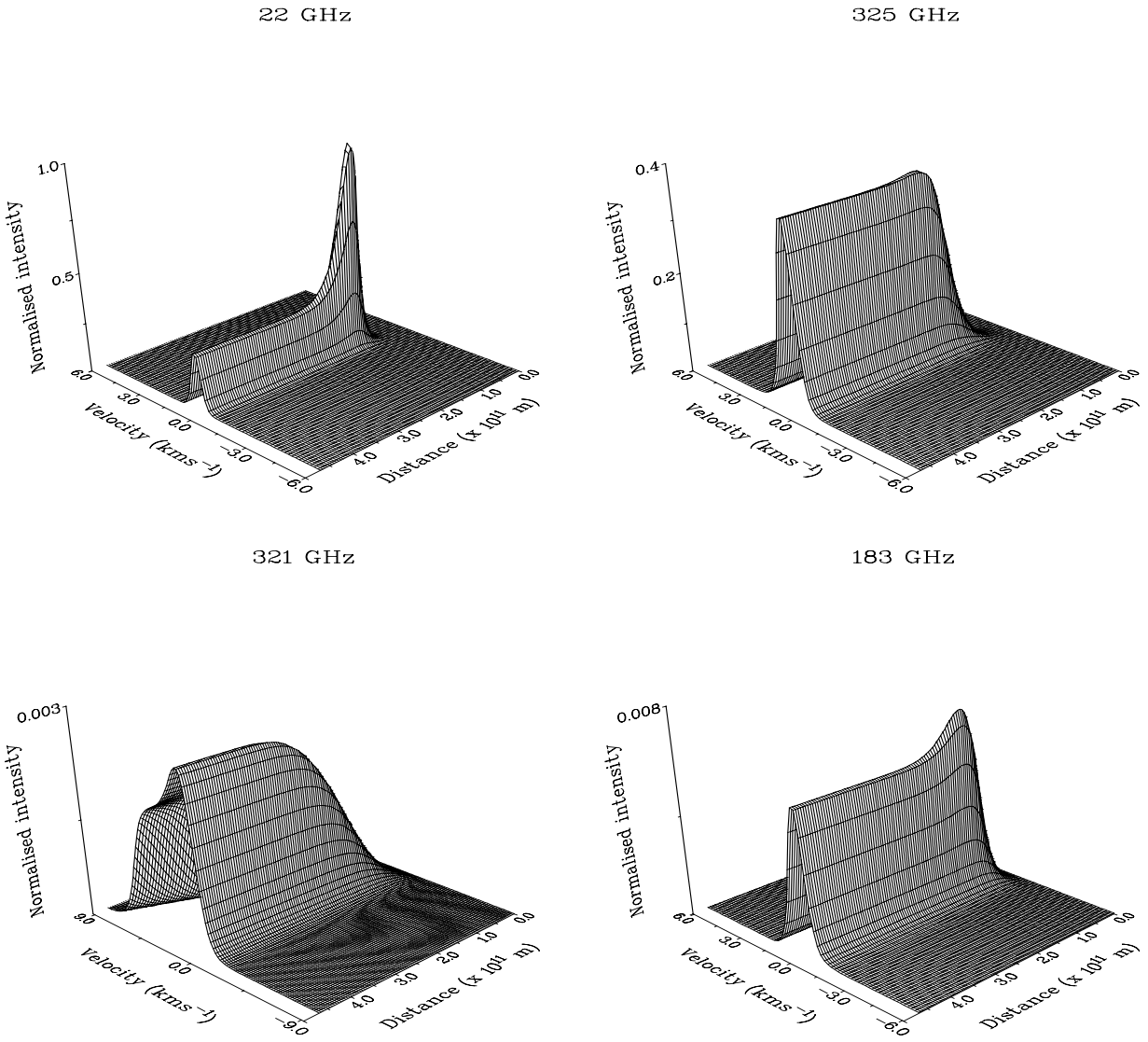

Fig. 2. Velocity-intensity-distance surfaces at 22, 325, 321 and 183 GHz for emission arising from a single masing component. For clarity, intensity has been normalised to the peak value in the 22 GHz surface. This component was chosen as it is particularly bright at 325 GHz. The physical conditions at this site in the CE are: $T_{\rm k} = 2070$ K; hydrogen number density, $n(\rm H_2) = 2.5 \times 10^9$ cm^{-3}; line-of-sight velocity gradient, $\alpha_{\rm los} = 4.5 \times 10^5$ km s^{-1} pc^{-1}.

The following method is used to treat the development of the component spectra over the propagation distance in the line-of-sight (see Eq. (1) of H96). At each numerical integration point in the propagation of masers through a masing zone, the molecular velocity distribution is divided into 101 bins covering 15 Doppler widths. The distribution is shifted appropriately in frequency at each integration step to take account of the local velocity field. Complete velocity redistribution (CVR) is assumed throughout the present calculations. This is achieved by summing the populations of all bins at each propagation step, taking account of saturation. The summed, possibly saturated, populations are then redistributed among the velocity bins according to a Gaussian profile. We note that the line centre of a component's spectral line does not correspond to the rest frequency of the maser transition in the presence of a velocity field. Microturbulence of velocity 1 km s^{-1} is added in quadrature to the Doppler linewidth.

3. Emitting components

Of the 3000 Monte Carlo sites distributed in the model CE, 44% yielded maser emission at 22 GHz; 49% at 325 GHz; 16% at 321 GHz and 87% at 183 GHz. The ranges of physical conditions which give rise to the five brightest components at each frequency are given in Table 3.

Any given component typically produces maser emission from several transitions. This is illustrated in Fig. 2, in which the propagation of masers through velocity-positional space is shown for a single emitting component. The saturation of all four masing lines is clearly evident

Table 5. Break down of the results by temperature. Total summed maser output lies in the ratio 5:3:4:1 for 22, 321, 325 and 183 GHz masers respectively.

Temperature Range (K)	<999	1000–1999	2000–2999	3000–3999	4000–4999	5000–5999	6000–6999
Frequency (GHz)	% Summed maser output at each frequency (number of contributing sites)						
22	<0.001 (245)	24 (752)	48 (250)	18 (40)	8 (14)	<2 (20)	<0.02 (1)
321	0	16 (183)	46 (231)	<24 (40)	9 (14)	5 (20)	0.2 (1)
325	<0.2 (430)	36 (716)	54 (249)	9 (37)	<0.5 (12)	<0.6 (19)	<0.05 (1)
183	19 (1608)	65 (716)	13 (244)	2 (37)	<0.5 (11)	0.5 (19)	<0.03 (1)

in Fig. 2. In the case of the 22 and 183 GHz emission, self-absorption of the maser photons also occurs. In the case of the 321 GHz maser line, a secondary emission shoulder arises from the effect of maser radiation transport under the CVR regime in the presence of a velocity gradient along the direction of maser propagation (cf. Field et al. 1994).

In our simulated data, the ranges of propagation and saturation distances, and the *FWHM* resulting for the five brightest components at each frequency are given in Table 4, and show that each of the bright components saturates at each frequency. Recalling that the maser propagation distance in the model is given by $3\Delta v_{\rm th}/|\alpha_{\rm los}|$, constrained to a maximum value of 3×10^{12} m, it is clear that at 22 GHz, the distance at which saturation sets in is between 1–2 $\Delta v_{\rm th}/|\alpha_{\rm los}|$. Bright 22 GHz maser components are saturated in our calculations, but weaker components may be unsaturated. For example, the brightest maser components at 183 GHz yield rather weak and unsaturated emission at 22 GHz.

With respect to observations of H_2O maser components at 22 GHz, these show that they have a typical linear size of 0.5 AU (7.5×10^{12} cm), with emission lines of *FWHM* typically $\sim$1 km s^{-1} (Bains 1995; Marvel 1997). From a brightness temperature analysis of the emission observed towards W Hya, Reid & Menten (1990) find that maser components are unsaturated in this Semi-Regular star. Observational evidence that masers may be close to saturation in Supergiants is given by Richards et al. (1999), who observed the spectral line *FWHM* of 22 GHz maser components narrowing with increasing brightness (the unsaturated regime) and rebroadening (under saturation).

Noting that the thermal linewidth for H_2O lines, say at 2000 K, is 2.1 km s^{-1}, the data in Table 4 show that our synthetic saturated component lineshapes may remain relatively narrow. Since, under the CVR regime, the rate at which population is redistributed over velocity is assumed to exceed the maser simulated emission rate, saturated rebroadening of the lineshapes does not occur (Goldreich & Kwan 1974). The narrowing of component lineshapes due to the initial unsaturated exponential amplification process is retained. Here, the broadest component *FWHM* result from the secondary gain effect (which does not require saturation) discussed above, rather than via saturated rebroadening. We are therefore unable to comment on this phenomenon in the present work. The lineshapes of H_2O maser components will be addressed in detail in future work.

In our simulations, it is also evident (see Table 3) that bright 22 GHz maser components may form within a few AU of the photosphere. However, observations by Reid & Menten (1997) indicate that electrons of sufficient density form a radio photosphere in Mira variables, which extends out to around 2 R_*. The sources of opacity which could be important at 22 GHz are proton-electron and H^- free-free bremsstrahlung. As these processes are not included in our model star, we estimate here the effect of a radio photosphere on our results by assuming that the opacity at 22 GHz will be greater than unity out to 2 R_* (2.2 AU in our model star). In fact, only a very small number of 22 GHz components (28 from a total of 1344) form within this radius in our model calculations. Neglecting these components from our data set would result in only a 0.02% reduction in total maser output at 22 GHz. Since the brightest of the components which lies within 2.2 AU achieves only 0.2% of the output of the brightest of all components at 22 GHz, these sites have a negligible effect upon our synthetic single-dish spectra and interferometry images. We therefore conclude that the inclusion of these opacity sources would have no significant influence on the outcome of our calculations.

We also note that the temperatures achieved in our model star are rather higher than those indicated by the observations by Reid & Menten (1997). This discrepancy is likely to be due to the lack of molecular coolants included in our model CE. In order to estimate the significance of the higher temperature regimes on our simulated data, we show in Table 5 a breakdown of our results by temperature. These data indicate that sites of $T_{\rm k} > 3000$ K produce a significant contribution to 22 and 321 GHz emission, whereas at 325 GHz and 183 GHz the higher temperature regions provide a more minor contribution. We note that the H_2O molecule is likely to be largely dissociated at 5000 K. As a general rule, for sites of $T_{\rm k} < 2000$ K, 22, 183 and 325 GHz emission tends to

be produced from roughly the same set of components. At higher temperatures, emitting components additionally tend to yield emission at 321 GHz. Other trends for emitting components are identified in Sect. 4.2.

4. Single-dish spectra

Figure 3 displays the spectra calculated for the stellar H_2O masers at 22, 321, 325 and 183 GHz. The synthetic lineshapes displayed in Fig. 3 are each composed of the emission from several hundred emitting components. In the case of the 22, 321 and 325 GHz masers however, emission from a relatively small number of sites dominates (see Sect. 5). We compare our synthetic lineshapes with the observational data below.

4.1. Observations

(i) Lineshapes observed for stars of low $\dot{M}$, such as M-Miras, tend to display a single dominant peak which occurs at the stellar velocity, to within a few km s^{-1}. The velocity extent of emission is typically $\sim$10 km s^{-1}. The 183 GHz maser generally displays the broadest lineshape, and that at 321 GHz the narrowest.
(ii) The peak intensities of the 22 and 325 GHz lineshapes are generally comparable. The 321 GHz lineshape tends to be weaker by a factor of 2–5 (Yates et al. 1995). In general, the 183 GHz lineshape is also weaker, by a factor of up to $\sim$12 for the Miras in González-Alfonso et al. (1998).
(iii) Some spectral features occur at similar velocities for all the maser transitions, suggesting that maser emission at different frequencies may originate from common regions of the CE. In particular, the 22 and 325 GHz maser line profiles often bear a strong resemblance (Yates et al. 1995).
(iv) Timescales for the variability of maser lineshapes vary between transitions. Change in peak intensity by a factor of 2 occurs most rapidly in 321 GHz masers (21 days), followed by 22 and 325 GHz masers (50 days) (Yates et al. 1996). The least variable are the 183 GHz profiles, which do not appear to alter significantly in intensity over time (González-Alfonso et al. 1998).

4.2. Simulations

(i) Synthetic line profiles also peak near the stellar velocity, to within $\pm$2 km s^{-1}. Velocity extents are within the range observed, although the broadest line profile is not that of the 183 GHz maser, as is typically observed.
(ii) The synthetic 22 GHz and 325 GHz line profiles are of comparable peak intensity, with the 321 and 183 GHz lineshapes less intense by a factor of $\sim$4. These values are consistent with the observations of Yates et al. (1995) and González-Alfonso et al. (1998).
(iii) The 22, 325 and 183 GHz lineshapes are of the same general form, with a single dominant feature peaking 1–2 km s^{-1} to the blue of V_*. In common with the 22 GHz profile, the 321 GHz lineshape displays another peak 1.5 km s^{-1} to the red of V_*. These similarities arise due to the spatial coincidence of different masers in the model CE. In particular, the following trends for emitting components influence the form of the single-dish spectra:
a) The most intense 183 GHz maser sites also produce fairly intense 325 GHz emission, but are weak at 22 GHz and weak/non-existent at 321 GHz. This leads to the similarity between the 325 GHz and 183 GHz line profiles evident in Fig. 3;
b) It is not unusual for 183 and 325 GHz emission to be entirely absent from masing clumps which are very bright at 321 GHz. These components also emit at 22 GHz, and form the feature to the red of V_* which is absent in the 325 GHz and 183 GHz spectra;
(iv) Variability appears to correlate with the number of emitting components contributing to the maser lineshape. The location of the sites in the model CE is also a likely factor, see Sect. 7.

5. Location of H_2O masers in the CE

In our simulated data, the location of the stellar H_2O maser sites which produced significant maser emission is shown in Figs. 4, 6, 7 and 8 for the 22, 321, 325 and 183 GHz masers respectively. In order to show the location of the brightest maser components in the plane of the sky, maser sites are marked by black circles centred on their projected positions. These circles have diameters which are linearly proportional to the intensity of a maser component integrated over the component spectral line profile ($\int I \, \mathrm{d}v$). At each frequency, we define $I_{\max}$ to be the maximum value of the velocity-integrated component intensity, denoted by $I_{\max,22}$, $I_{\max,321}$, $I_{\max,325}$ and $I_{\max,183}$. The stellar disk, of radius 1.1 AU at this epoch, is represented by the grey disk at $(0,0)$. Note that the figures are not plotted to the same scale. The largest diameter in each plot corresponds to the $I_{\max}$ at that particular frequency and diameters are not scaled between plots. The ratio of $I_{\max,22}$:$I_{\max,321}$:$I_{\max,325}$:$I_{\max,183}$ is 85:269:48:1 respectively.

5.1. 22 GHz masers

Around half (44%) of the three thousand Monte Carlo sites initially distributed in the CE yielded 22 GHz maser emission in the line-of-sight. Bright components ($I_{22} > 0.1\ I_{\max,22}$) lie in an irregularly-shaped distribution in Figs. 4a,b within 9 R_* (10 AU) of the star, with very low gain emission extending much further. No strong emission originates from regions over the stellar disk, indicating that bright 22 GHz masers amplify tangentially in the model CE. A requirement for producing strong maser emission is that long amplification paths are available. The tangential velocity gradients in the 22 GHz maser zone are typically significantly less than those along radial paths, see Table 3.

The extent and spatial structure of the calculated 22 GHz images agree with those of many Mira

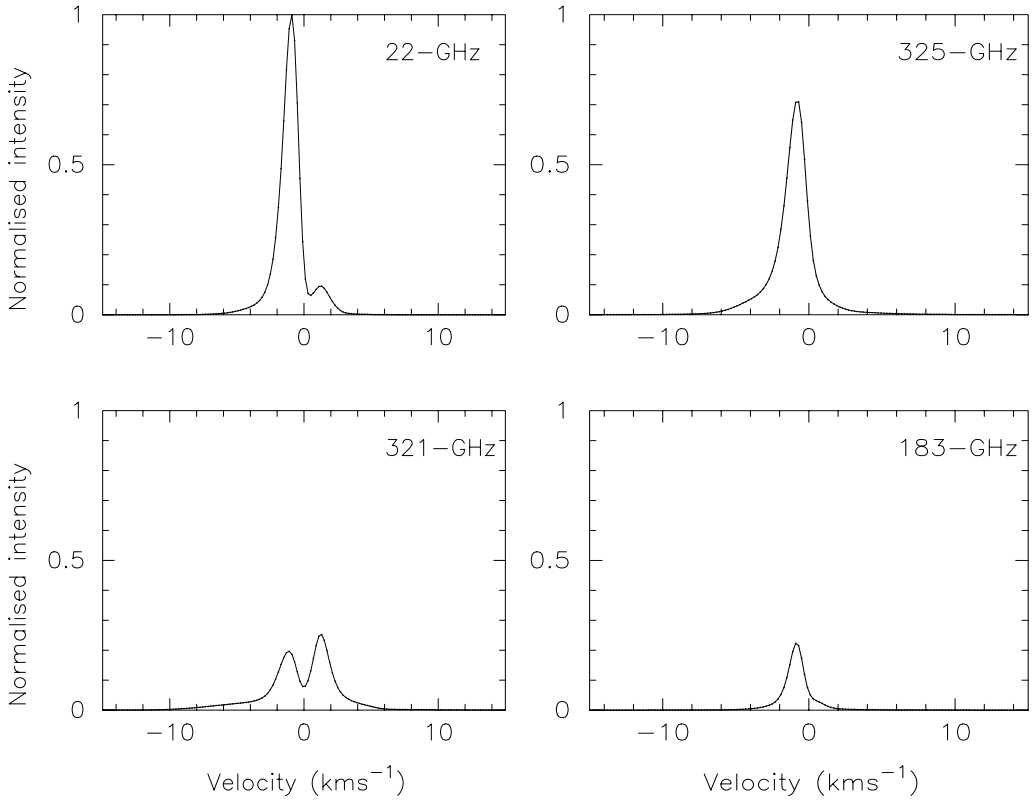

Fig. 3. Calculated lineshapes at 22, 321, 325 and 183 GHz. Lineshape specific intensity is normalised to the peak value at 22 GHz.

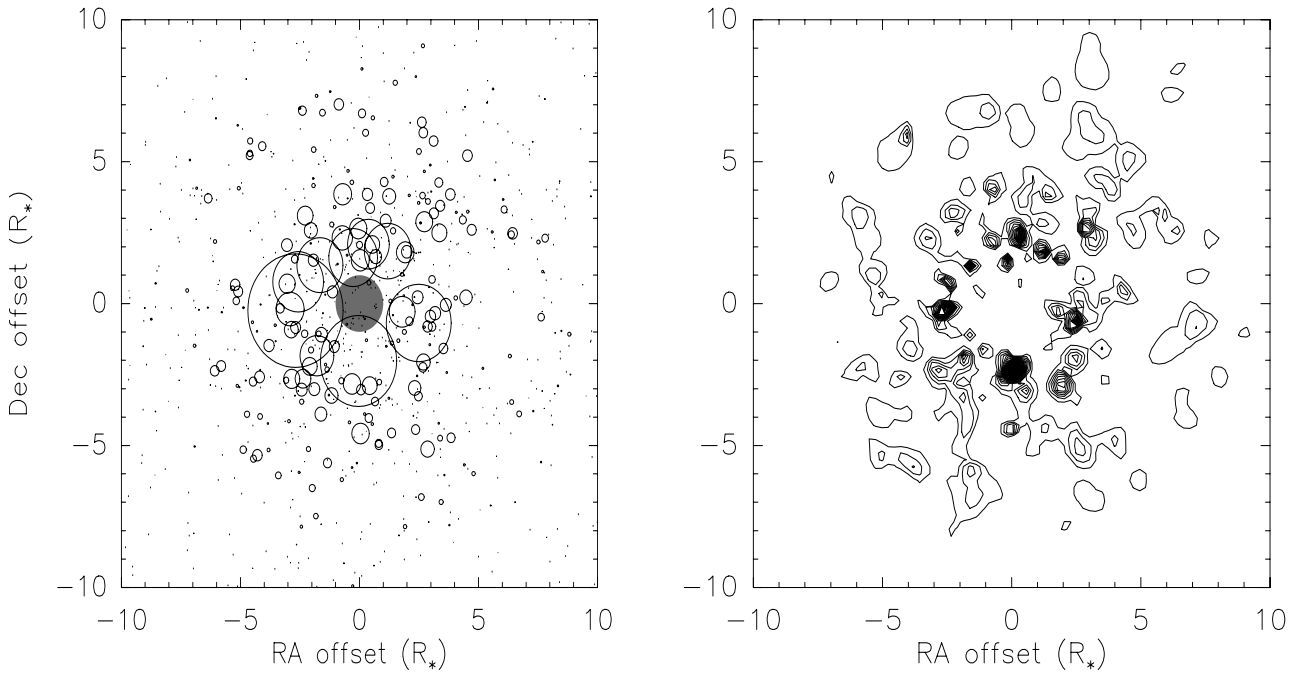

Fig. 4. H_2O masers in the $6_{16} \rightarrow 5_{23}$ transition at 22 GHz generated in the CE of the model M-Mira. **a)** Intensities of the masers are linearly proportional to the diameters of the black circles shown. Circles are centred on the maser projected coordinates. The grey disk represents the stellar disk. **b)** The same data is redrawn as a contour plot, where the lowest contour is set at 1% of the maximum in the plot. The levels are clipped in order to represent the brightest maser emission.

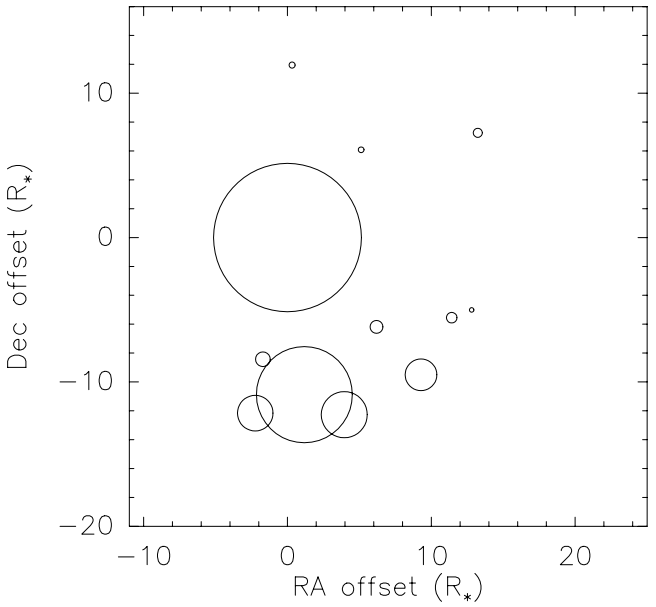

Fig. 5. VLA data for R Cas from Table 6 in Colomer et al. (2000). Here spot diameter is plotted proportional to velocity-integrated intensity and the linear offset scale is calculated using a Hipparcos distance to R Cas of 106.7 pc (Whitelock & Feast 2000). The mean photospheric diameter of R Cas is 28.6 ± 3.9 mas for fundamental mode pulsation (Haniff et al. 1995). The stellar position is unknown in this figure.

observations (see e.g. Marvel 1997; Colomer 2000), noting that the results should be compared with objects of similar $\dot{M}$. In this connection we show observations of 22 GHz emission detected towards R Cas using the VLA by Colomer et al. (2000) in Fig. 5. With a period of 430 days, a stellar radius of 1.5 ± 0.2 AU (Haniff et al. 1995) and a $\dot{M} = 3.4 \times 10^{-7}\ M_\odot\ \mathrm{yr}^{-1}$ (Truong-Bach et al. 1999), R Cas is a M-Mira fairly similar to our model star of $\dot{M} = 1.8 \times 10^{-7}\ M_\odot\ \mathrm{yr}^{-1}$ and $R_* = 1.1$ AU.

In the R Cas observations, the H_2O maser distribution is represented in terms of 12 Gaussian sources occupying a spatial extent of 15×9 R_* (23×13 AU). The computed image and the observational image are similar in appearance in that the total maser output is dominated by a few bright components/blends of components in an irregularly shaped distribution. In the observed image, the minimum component $\int I\ \mathrm{d}v$ which occurs within the 23×13 AU extent is $0.03\ I_{\mathrm{max,obs}}$. In the calculated image, components of $0.03\ I_{\mathrm{max},22}$ occur out to a similar extent of diameter 25.2 AU. However, in the calculated image, this includes emission from 157 Monte Carlo sites rather than around 12, suggesting that we may have oversampled our model CE. Alternatively, large numbers of components may be blended together in the VLA observations, or the low intensity sites could be obscured by noise.

The projected positions of the 22 GHz maser components are related to their location in the CE model in Fig. 9. Figure 9a shows that the peak in the radial distribution of 22 GHz emission occurs at 2.7 R_*, with secondary peaks at both 4.5 and 7.3 R_*. The physical conditions in these regions are shown in Figs. 9b, c and d. All components of intensity $>0.01\ I_{\mathrm{max},22}$ occur within 13.6 R_* of the stellar position. However, extremely weak "diffuse" emission, of intensity as low as $2 \times 10^{-6}\ I_{\mathrm{max},22}$, extends much further, out to a radius of 25.5 R_* in the case of 22 GHz masers.

A wide range of physical conditions evidently gives rise to population inversion in the $6_{16} \rightarrow 5_{23}$ transition. However the highest gain masers occur in relatively high temperature and high density regions, see Table 3. Some of these conditions lie outside of the parameter space investigated by both Y97 and Neufeld & Melnick (1991). In the model CE, bright emission commonly occurs from components with higher kinetic temperatures than those considered in previous water maser models. We note that these higher temperatures appear to be in conflict with observations by Reid & Menten (1997). In this connection, very recent oxygen-rich hydrodynamical stellar models by Höfner (private communication) do not show such high temperature spikes. The use of such models in future work should yield results which are more compatible with these observations.

Figure 9b shows that our simulated 22 GHz masers occur in the region of the CE in which acceleration of circumstellar material yields the steadily-outflowing stellar wind, as observed e.g. by Richards et al. (1996). Model component lifetimes can be roughly estimated by the crossing time required to traverse this zone. At an average outflow velocity of 4 $\mathrm{km\,s}^{-1}$, a bright component travelling from around 2 to 12 AU in the CE survives 12 years. Component proper motions should be therefore be of the order 0.85 AU yr^{-1} in stars of low $\dot{M}$.

5.2. 321 GHz masers

A small minority of Monte Carlo sites (16%) produced maser emission at 321 GHz. Figure 6 shows that, in the projected map, the brightest 321 GHz maser components occur within 3.5 R_* (4 AU) of the stellar position. It is also evident from Fig. 6 that no bright 321 GHz emission orginates from regions directly in front of the stellar disk, indicative of a tangential amplification process. We note that 321 GHz components may achieve greater intensity than those of the other masers discussed here. At this epoch of our calculations, $I_{\mathrm{max},321}$ exceeds $I_{\mathrm{max},22}$ by a factor of three.

Turning to the location of 321 GHz masers in the model CE, Fig. 9a shows that the peak in the radial distribution of 321 GHz maser emission occurs between ∼2–3.5 R_*. Again it is the combination of suitable pumping conditions, in conjunction with a low line-of-sight velocity gradient, which produces a high gain maser of long amplification path. Bright 321 GHz maser components are the rarest of all the four masers discussed here. Only thirty-three sites of $I_{321} > 0.01\ I_{\mathrm{max},321}$ resulted from our calculations, existing out to 4.5 R_* in the CE.

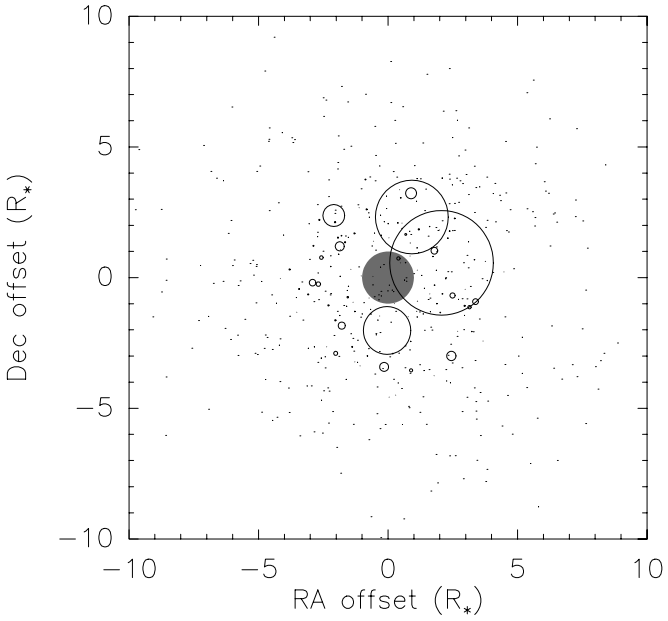

Fig. 6. 321 GHz emission calculated at this epoch. See caption of Fig. 4 for more details.

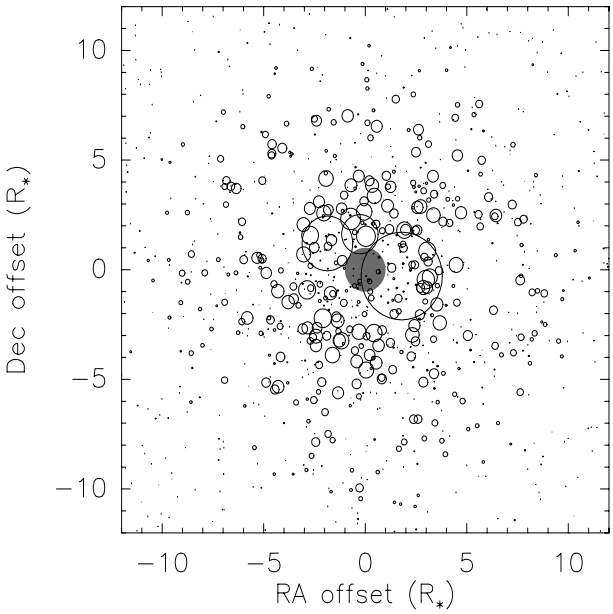

Fig. 7. As for Fig. 4 but for 325 GHz emission. See Sect. 5.3 for details.

The remaining, very weak emission is contained within a radius of 11.3 R_*.

In summary, it is clear that very few sites in the model CE are suitable for producing strong 321 GHz emission. These sites probe the very innermost region of the CE, a region also probed by SiO masers (see H96). This result is unsurprising since the E_u of the 321 GHz H_2O transition is very similar to that of $v = 1$ SiO masers, both lying at around 1800 K above ground state. Further calculations are required in order to determine whether 321 GHz maser emission may be originating from the same volumes of gas as those giving rise to bright SiO masers. Given that the $10_{29} \rightarrow 9_{36}$ transition lies at a relatively high energy, it follows that 321 GHz maser emission requires conditions of high gas density, temperature and radiation field energy density, and that it is not pumped by the larger range of conditions which leads to 22 GHz maser emission in the CE. Y97 also identifies a relatively restricted range of conditions over which the 321 GHz maser transition is strongly inverted.

5.3. 325 GHz masers

The number of sites contributing to 325 GHz emission is similar to that of 22 GHz maser emission (49%). At this epoch, Fig. 7 shows that the brightest 325 GHz maser components occur within a radius of 11 R_* (12 AU) of the stellar position in the projected map. The stellar disk is partially obscured in Fig. 7, but no bright emission occurs from over the star. Tangential amplification is prevalent, as for the 22 and 321 GHz masers.

In the CE model, very weak emission extends to a radius of 30 R_* from the stellar position, with sites of >0.01 $I_{\max,325}$ occurring out to a radius of 18 R_*. In Fig. 9a it is clear that bright 325 GHz emission occurs over a similar region of the CE to that occupied by 22 GHz masers. Although $I_{\max,22}$ exceeds $I_{\max,325}$ by a factor of around two at this epoch, there is a higher success rate of producing masers at 325 GHz both than at 22 and 321 GHz. The observed strength of the 325 GHz maser is due to a large number of maser spots of moderate intensity, rather than a few very bright maser components. The 325 GHz maser can exist out to larger radial distances than both the 22 GHz and 321 GHz masers, indicating it can be pumped in regions of lower gas density and temperature. The transition which must be inverted to produce this maser is relatively low-lying, with an E_u of 470 K above ground state.

5.4. 183 GHz masers

A large majority of sites (87%) produced masers at 183 GHz. Figure 8 shows the projected spatial structure of emission predicted by our simulations. Compared with the other masers discussed in the present work, the radial distribution of 183 GHz emission is very extended. Sites of >0.01 $I_{\max,183}$ exist out to 35 R_* (39 AU), with weak emission extending out to a radius of 48 R_*. Unlike the other masers discussed here, both radial and tangential amplification is evident for the 183 GHz emission. For components lying relatively far from the star, the tangential velocity gradient may exceed that in the radial direction, see Table 3 and Fig. 9b.

An additional feature of the 183 GHz maser morphology, unlike that of the other stellar H_2O masers, is that emission is not dominated by a small number of very

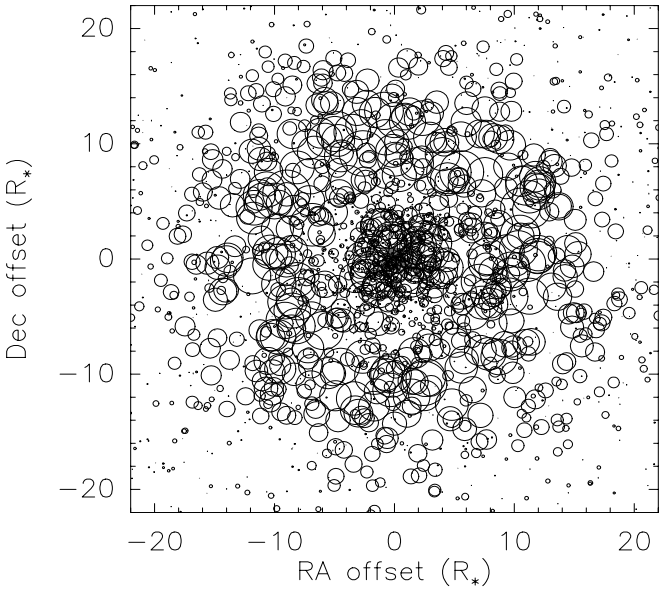

Fig. 8. As for Fig. 4 but for 183 GHz emission. See Sect. 5.4 for details.

intense components. Rather, the strength of this maser is provided by a large number of contributing components of similar, weak intensity: $I_{\rm max,22} > I_{\rm max,183}$ by a factor of 85. Figure 9a shows how 183 GHz emission is more evenly distributed over radius than the 22, 321 and 325 GHz maser emission.

The upper level of the $3_{13} \rightarrow 2_{20}$ 183 GHz transition lies at an energy of 205 K above ground state. The physical conditions leading to the brightest 183 GHz emission are shown in Table 3. A regime of low $T_{\rm k}$ and $n(H_2)$ favours 183 GHz emission, and the maser may therefore be pumped in regions relatively far from the star. However, the transition can also be inverted in a high kinetic temperature and density regime. These pumping conditions are in agreement with the results of Y97, in which the 183 GHz maser transition was found to be strongly inverted over a large range of conditions of low $T_{\rm k}$ with low $n(H_2)$ and of high $T_{\rm k}$ with high $n(H_2)$. The region of the CE occupied by the brightest 183 GHz components is shown in Figs. 9b, c and d.

6. Predictions of new stellar H_2O masers

Some transitions which produce strong maser emission in the model have never been detected towards stellar environments. Many have been predicted by other models, for example those of Neufeld & Melnick (1991) and Y97. However, these models did not predict the line profiles and images expected for new masers. Some examples of predicted maser lineshapes are shown in Fig. 10. The lines are considered to be of an observable strength as they have intensities comparable to, and sometimes higher than, the 22, 321 and 325 GHz masers at the same epoch, see Fig. 3. The transitions which must be inverted to

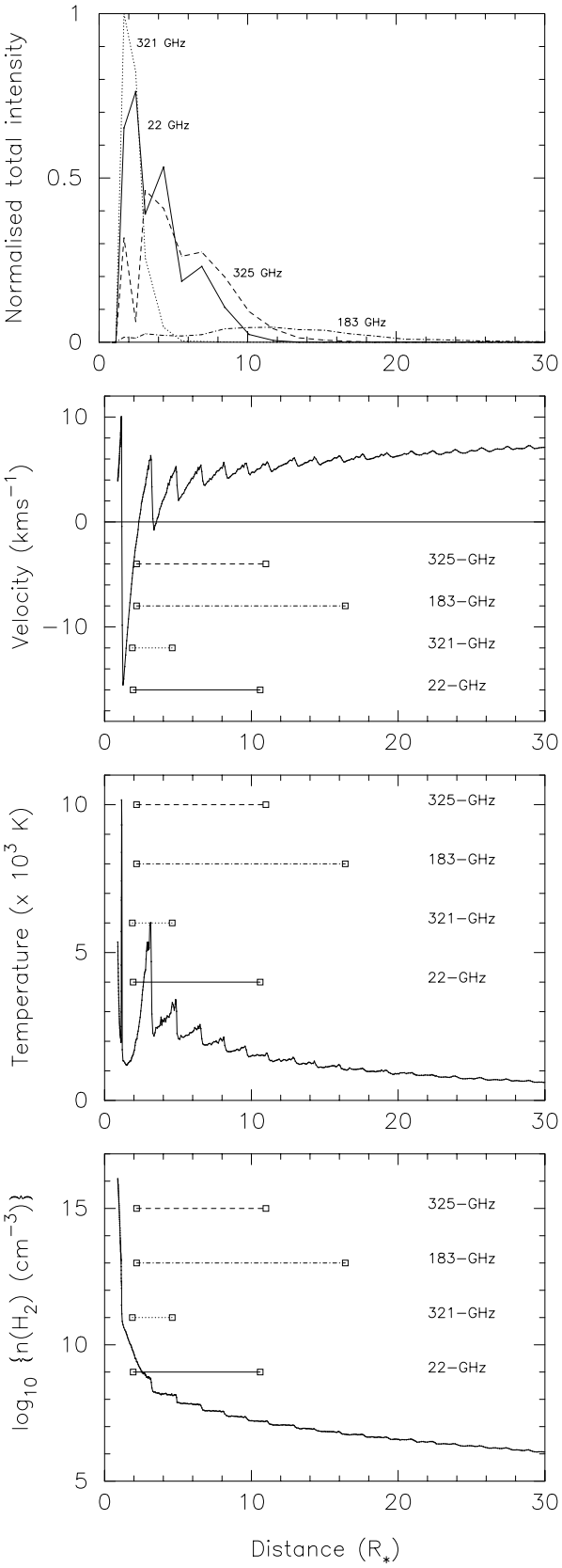

Fig. 9. The physical conditions giving rise to bright emission at the epoch of our calculations. **a)** Radial distribution of maser emission; **b)** gas velocity as a function of radial distance; **c)** $T_{\rm k}$; **d)** $n(H_2)$. Marked on the plots are the radial extents of the brightest 10% of components produced by the model at 325, 183, 321 and 22 GHz.

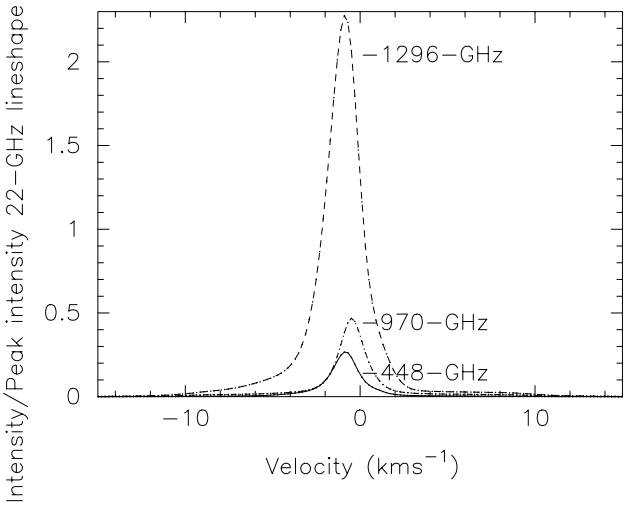

Fig. 10. Some maser lineshapes predicted by the model at 1296, 970 and 448 GHz. The lineshape intensity is normalised to the peak intensity of the 22 GHz maser lineshape in Fig. 3.

produce the new masers are listed in Table 6. Noting that many H_2O lines are obscured by atmospheric attenuation, we provide an indication of those masers which may be observable by satellite missions such as the Herschel Space Observatory (HSO). We discuss the spatial structure of such masers in Sect. 7.

7. Classification of stellar H_2O masers

The spatial structure and temporal variability of the observed and predicted stellar H_2O masers fall into three groups, broadly characterised by the energy of the upper level, E_u, of their transitions.

Table 6. The stellar H_2O masers predicted by our simulations.

Frequency (GHz)	Transition	E_u (K)	Observable by the HSO?
*380	$4_{14} \rightarrow 3_{21}$	324	N
448	$4_{23} \rightarrow 3_{30}$	433	N
970	$5_{24} \rightarrow 4_{31}$	599	Y
1322	$6_{25} \rightarrow 5_{32}$	796	N
1158	$6_{34} \rightarrow 5_{41}$	935	Y
1542	$6_{33} \rightarrow 5_{42}$	953	Y
1441	$7_{26} \rightarrow 6_{33}$	1022	Y
1766	$7_{35} \rightarrow 6_{42}$	1176	Y
1296	$8_{27} \rightarrow 7_{34}$	1275	N
2245	$8_{36} \rightarrow 7_{43}$	1449	N
906	$9_{28} \rightarrow 8_{35}$	1556	Y
2532	$9_{37} \rightarrow 8_{44}$	1751	N
2575	$10_{38} \rightarrow 9_{45}$	2082	N

* Already observed towards a star-forming region.

7.1. Group I: masers typically of $E_u > 950$ K

In the CE model, these masers are calculated to be similar in spatial structure to the 321 GHz maser, see Fig. 6. The strongest emission occurs in a single dominant region, mostly within 5.5 R_* of the model star. This category includes the 906, 1296, 1322 (an exception as it has E_u = 796 K), 1441, 1766, 2245, 2532 and 2575 GHz masers. These masers have a very restricted range of possible pumping conditions in the circumstellar environment and occur in regions close to the star, in regions of high gas density and dense stellar radiation field. In Group I masers, the total maser flux observed towards the source depends on a small number of very bright masers, rather than a large number of weaker components. Only a small percentage of maser sites produce emission in the line-of-sight, typically <20% of the initial Monte Carlo sample. The maximum velocity-averaged flux of a maser spot in these transitions is larger than that of masers from Group II and III in general by 1–2 orders of magnitude respectively. If the physical conditions at only a few maser sites change such that emission at these sites is significantly weakened, this will have a dramatic effect on total maser brightness observed towards the source. These masers also are located in the innermost region of the CE, the region most affected by the passage of shocks. It is therefore expected that these masers will have the most dramatic temporal variability of the stellar H_2O masers, as observed for 321 GHz masers by Yates & Cohen (1996).

7.2. Group II: masers of 450 K $< E_u <$ 950 K

These masers resemble the 22 GHz and 325 GHz masers. They tend to have radial emission distributions which peak at around 3 and 7 R_* in the CE model, see Fig. 9. These are the 970 and 1158 GHz masers. These masers have upper transition levels in the range 450–950 K and are pumped out to regions of lower density and of a more diluted stellar radiation field than the masers in Group I. The number of maser components calculated to emit in the line-of-sight is ≥25% and less than 50% of the possible total. The maximum averaged flux of the spots is moderate relative to that in Group I. The relatively large number of sites, extending over a large region of the CE, suggests that the loss of maser emission from a few sites is not likely to have a significant effect on the total maser output from the source. Also, maser components exist both within and outside of the region most disrupted by shocks. These masers are therefore predicted to show a lesser degree of temporal variability than the Group I masers, as observed by Yates & Cohen (1996). Yates & Cohen (1996) also noted that 22 and 325 GHz masers do not vary synchronously, however. This could be due to the fact that the peaks in the radial distribution of maser emission are not coincident for the different frequencies. We would expect 22 GHz masers to show the effect of a shock wave traversing the CE first, as the maximum in the radial

distribution of maser intensity is nearer to the photosphere than that of the 325 GHz maser.

7.3. Group III: masers of $E_u < 450$ K

The 380 GHz and 448 GHz masers resemble the 183 GHz maser. As for the 183 GHz maser, these masers occupy large extents in the CE, with relatively weak emission extending out to radii of 18–27 R_*. It is clear that these masers, which originate from the most low-lying energy levels, can be pumped by regions of much lower density and temperature than their Group I and II counterparts, as well as by the higher temperature and density regime closer to the star. This explains the large number of maser sites producing emission at these frequencies, which is >60%. The maximum averaged component flux in each transition is less than that of the masers in Group II typically by an order of magnitude. As the loss of emission from these transitions at a few sites would not produce a significant effect on the maser output or spatial structure, temporal variability is expected to be the lowest in these masers. This corresponds well to the observational results of González-Alfonso et al. (1998) in which the intensity of 183 GHz maser lineshapes appears to remain very stable. However, in stars of similar mass loss rate to our model, the lineshape peak can shift in velocity to either side of V_* between observational epochs. This is also the case for SiO maser lineshapes. We require variability calculations in order to understand this behaviour.

8. Summary

We set out to simulate H_2O maser emission in the circumstellar environment of a M-Mira variable, compare our results qualitatively with observations and discuss them in terms of the physical conditions prevailing in the CE. The combination of an H_2O maser saturation radiation transport model with a M-Mira CE pulsation model has resulted in:

1. Synthetic single-dish lineshapes at 22, 183, 321 and 325 GHz which have velocity extents consistent with those observed. Singly-peaked profiles are reproduced for 22, 325 and 183 GHz maser emission, as observed for stars of similar $\dot{M}$ to our model star. The ratio of the peak synthetic lineshape intensities is comparable to those observed.
2. A synthetic 22 GHz image which has an asymmetric distribution of bright components within a spatial extent typical of observations towards Miras. Our simulations confirm that bright 22 GHz emission originates from a zone in which material is undergoing acceleration away from the star, as observed.
3. A prediction of the spatial structure of 183, 325 and 321 GHz masers in the CE. We find that these masers occupy overlapping regions in the CE, with the 321 GHz masers originating from the same region as SiO masers. We attribute the observed variability characteristics of these masers to their very different extents in the CE, and the difference in the number of bright components contributing to the total emission for each transition.
4. A prediction of the existence of new, bright stellar masers. The lineshapes and spatial structure of these masers in the CE have been calculated, on the basis of which we are also able to predict their variability. Future experiments using ALMA and the HSO may allow verification of these predictions.

An important result of these simulations is that bright maser emission often occurs from physical conditions which have not been explored by previous H_2O maser models. These aimed to find the optimum conditions for H_2O maser emission, rather than input conditions from advanced stellar models. We find here that bright maser emission can occur from hotter regions than those previously considered, of $T_k > 2000$ K, although we note that the presence of higher temperatures in the H_2O maser zone is uncertain. In addition, propagation of maser emission including velocity-shifts along the line-of-sight plays a crucial role in deciding which maser components in the CE will achieve very high intensities.

Finally, it is striking that these simulations reproduce both the stellar SiO (see H96) and H_2O maser properties. This numerical experiment shows that a mechanism of pulsation and dust radiation pressure for driving AGB mass loss is qualitatively consistent with observed stellar SiO and H_2O maser data.

Acknowledgements. We thank the Swedish Foundation for International Cooperation in Research and Higher Education (STINT) for the financial support of E. M. L. H. This work was carried out on the Miracle supercomputer, at the HiPerSPACE Computing Centre, UCL, which is funded by the UK Particle Physics and Astronomy Research Council. We thank the referee Dr. M. Reid for his significant contributions to this paper.

References

Bains, I. 1995, M.Sc. Thesis, University of Manchester
Bayley, M. 1985, Ph.D. Thesis, University of Bristol
Bowen, G. H. 1988, ApJ, 329, 299
Bowers, P. F., & Johnston, K. 1994, ApJS, 92, 189
Chapman, J. M., & Cohen, R. J. 1986, MNRAS, 220, 513
Colomer, F., Reid, M. J., Menten, K. M., & Bujarrabal, V. 2000, A&A, 355, 979
Cooke, B., & Elitzur, M. 1985, ApJ, 295, 175
Doel, R. C., Gray, M. D., Humphreys, E. M. L., Braithwaite, M. F., & Field, D. 1995, A&A, 302, 797
Field, D., & Gray, M. D. 1988, MNRAS, 234, 353
Field, D., Gray, M. D., & de St. Paer, P. 1994, A&A, 282, 213
Goldreich, P., & Kwan, J. 1974, ApJ, 190, 27
González-Alfonso, E., & Cernicharo, J. 1999, ApJ, 525, 845
González-Alfonso, E., Cernicharo, J., Alcolea, J., & Orlandi, M. A. 1998, A&A, 334, 1016
Gray, M. D., Humphreys, E. M. L., & Field, D. 1995, Ap&SS, 224, 63

Green, S., Maluendes, S., & McLean, A. D. 1993, ApJS, 85, 181
Haniff, C. A., Scholz, M., & Tuthill, P. G. 1995, MNRAS, 276, 640
Humphreys, E. M. L., Gray, M. D., Yates, J. A., et al. 1996, MNRAS, 282, 1359 (H96)
Laor, A., & Draine, B. T. 1993, ApJ, 402, 441
Lewis, B. M. 1989, ApJ, 338, 234
Marvel, K. 1997, PASP, 109, 1286
Menten, K. M., & Melnick, G. J. 1991, ApJ, 377, 647
Menten, K. M., Melnick, G. J., Phillips, T. G., & Neufeld, D. A. 1990, ApJ, 363, L27
Neufeld, D. A., & Melnick, G. J. 1991, ApJ, 368, 215
Reid, M. J., & Menten, K. M. 1990, ApJ, 360, L51
Reid, M. J., & Menten, K. M. 1997, ApJ, 476, 327
Richards, A. M. S., Yates, J. A., & Cohen, R. J. 1996, MNRAS, 282, 665
Richards, A. M. S., Yates, J. A., & Cohen, R. J. 1999, MNRAS, 306, 954
Takaba, H., Ukita, N., Miyaji, T., & Miyoshi, M. 1994, PASJ, 46, 629
Truong-Bach, Sylvester, R. J., Barlow, M. J., et al. 1999, A&A, 345, 925
Whitelock, P., & Feast, M. 2000, MNRAS, 319, 759
Yates, J. A., & Cohen, R. J. 1994, MNRAS, 270, 958
Yates, J. A., & Cohen, R. J. 1996, MNRAS, 278, 655
Yates, J. A., Cohen, R. J., & Hills, R. E. 1995, MNRAS, 273, 529
Yates, J. A., Field, D., & Gray, M. D. 1997, MNRAS, 285, 303 (Y97)